



Cite this: *Nanoscale*, 2014, **6**, 12426

Received 5th August 2014,
 Accepted 2nd September 2014

DOI: 10.1039/c4nr04488f

www.rsc.org/nanoscale

Stable 4 V-class bicontinuous cathodes by hierarchically porous carbon coating on $\text{Li}_3\text{V}_2(\text{PO}_4)_3$ nanospheres†

Linfeng Fei,^{‡a} Li Sun,^{‡b} Wei Lu,^a Min Guo,^a Haitao Huang,^a Jiaping Wang,^b Helen L. W. Chan,^a Shoushan Fan^b and Yu Wang^{*a}

A high performance, durable cathode material for lithium ion batteries is achieved by incorporating ~50 nm $\text{Li}_3\text{V}_2(\text{PO}_4)_3/\text{C}$ core-shell nanospheres into a porous carbon framework. The $\text{Li}_3\text{V}_2(\text{PO}_4)_3/\text{C}$ nanocomposite delivers an initial discharge capacity of 130 mA h g⁻¹, approaching its theoretical limit (133 mA h g⁻¹). At a high current rate (10 C), the nanocomposite displays an impressive long cycle life and remarkable capacity retention (90% after 1200 cycles). Notably, the Coulombic efficiency is above 99% during the course of cycling. The remarkable power capability and cycle stability derived from our simple and scalable synthesis suggests that this 4 V-class material could be one of the most promising candidates for future batteries.

Introduction

Lithium ion batteries (LIBs) are one of the most successful energy storage systems for a wide range of modern applications including electrical vehicles and consumer electronics due to a relatively high energy density, high power, and long lifespan.^{1–3} At present, unprecedented research efforts have been made and supported by many nations on seeking new-fashioned cathode materials, which are of critical importance in determining the whole battery performance.⁴ Amongst all prospective cathode materials for next-generation LIBs, monoclinic $\text{Li}_3\text{V}_2(\text{PO}_4)_3$ is particularly appealing due to its excellent structural stability brought by a three-dimensional polyanion $(\text{PO}_4)^{3-}$ framework as well as a high redox potential (average potential of ~4 V vs. Li^+) when compared to that of well-developed LiFePO_4 (~3.4 V).^{5–9} Notably, $\text{Li}_3\text{V}_2(\text{PO}_4)_3$ is one of the few

4 V-class polyanion-based cathode materials (see Fig. S1,† comparison of several cathode materials),^{10–12} and due to the safety, toxicity and price concerns of the current LiCoO_2 cathode, there has been an increasing pursuit of 4 V-class electrode materials around the world to replace LiCoO_2 . However, the inferior electronic conductivity (σ , 2.0×10^{-8} S cm⁻¹) of $\text{Li}_3\text{V}_2(\text{PO}_4)_3$ arise from its inherently separated VO_6 octahedral arrangement (Fig. S2†) in the crystal structure has greatly limited its application potential.^{5,7,9} Consequently, $\text{Li}_3\text{V}_2(\text{PO}_4)_3$ -based LIBs often deliver limited high-rate capability and suffer from severe capacity fading after repeated charging/discharging cycles in practice.

Existing strategies to deal with the above shortcoming so as to enhance the electrochemical performance of polyanion-based materials have mostly focused on powder size reduction and conductive surface coating.^{2,11,13} Through size reduction, powders are reduced to nanosize dimensions which simultaneously shortens the distance for Li^+ transport across the particular electrode and increases the electronic contact area between the electrode and the electrolyte, leading to full access of their theoretical capacity as well as a longer cycle life.¹⁴ Nevertheless, nanosized materials are generally synthesized *via* low-temperature methods and because of this, the resulting crystallinity is relatively low and hence, reduces the electrochemical stability.¹³ Another issue associated with the size reduction is that owing to their high surface energy, nanomaterials are often favored to be self-aggregated in ordinary batteries, yielding a very large surface area loss. For the reasons mentioned, it remains a challenge to fully utilize the advantages of nanosized active materials. Another feasible technique for improving the performance of cathode materials is through conductive coating. This method involves coating of a conductive layer (*e.g.* carbon, RuO_2 , graphene, conductive polymers, *etc.*) on the active material to modify the surface chemistry and to construct more efficient electron pathways.^{6,15–18} Among the coating materials used, a vast majority of work has been concentrated on carbon coating for its economical and practical features (such as high electrical conductivity, excellent chemical/electrochemical stability, low

^aDepartment of Applied Physics and Material Research Center, The Hong Kong Polytechnic University, Hong Kong SAR, China. E-mail: yu.wang@polyu.edu.hk

^bDepartment of Physics and Tsinghua-Foxconn Nanotechnology Research Center, Tsinghua University, Beijing 100084, China

† Electronic supplementary information (ESI) available: Comparison of current cathode materials, comparison of the electrochemical performance among $\text{Li}_3\text{V}_2(\text{PO}_4)_3$ -based cathode materials, supplementary figures. See DOI: 10.1039/c4nr04488f

‡ These two authors contributed equally to this work.

cost, *etc.*) and in fact, carbon coating has been frequently applied on $\text{Li}_3\text{V}_2(\text{PO}_4)_3$.^{5,6,9,12,19–24} Despite the fact that experimental results have proven the use of an ideal core-shell carbon coating (*i.e.* to homogeneously distribute a thin carbon layer on the surface of the host material particles) could successfully enhance the electrochemical performance of cathode materials, it would be difficult to achieve perfect carbon coating both technically and cost-effectively, preventing the application in scalable manufacturing.¹⁵

To address the above-mentioned issues, we propose a rational design of $\text{Li}_3\text{V}_2(\text{PO}_4)_3$ -based cathode materials meeting the following criteria: (i) fine-sized and highly-crystallized $\text{Li}_3\text{V}_2(\text{PO}_4)_3$ particles to guarantee stable cathodic performance; (ii) a conductive coating on $\text{Li}_3\text{V}_2(\text{PO}_4)_3$ particles to improve its electronic conductivity and to prevent structure degradation upon cycling; (iii) a conductive matrix to ensure dispersive distribution (to avoid self-aggregation) of $\text{Li}_3\text{V}_2(\text{PO}_4)_3$ particles and to offer a three-dimensional (3D) continuous electron pathway; (iv) sufficient porosity in the matrix to benefit electrolyte infiltration; and (v) adopting a facile synthesizing approach if possible for future large-scale applications. To the best of our knowledge, no attempt has been made to create $\text{Li}_3\text{V}_2(\text{PO}_4)_3$ -based cathode materials for LIBs satisfying the above conditions. Herein, we contribute to this work by creating a novel $\text{Li}_3\text{V}_2(\text{PO}_4)_3$ -carbon composite material that combines the advantages of hierarchical porous carbon and nanometer-sized $\text{Li}_3\text{V}_2(\text{PO}_4)_3$ active particles. A superior hybrid material was obtained by incorporating conformally carbon-coated, well-crystallized $\text{Li}_3\text{V}_2(\text{PO}_4)_3$ nanospheres ($\text{Li}_3\text{V}_2(\text{PO}_4)_3/\text{C}$ core-shell nanospheres) inside micrometer-sized 3D porous carbon networks. This hierarchical nanostructured $\text{Li}_3\text{V}_2(\text{PO}_4)_3/\text{C}$ (hereafter abbreviated as HN-LVP@C) configuration smartly unites multiple beneficial features including highly-crystallized and single-crystalline

$\text{Li}_3\text{V}_2(\text{PO}_4)_3$ nanospheres to stabilize the electrochemical cycling, a well-connected 3D conductive framework, a well-developed meso-macroporous microstructure to facilitate electrolyte infiltration, and abundant porous space for accommodating volume expansion during electrode charge/discharge. The final HN-LVP@C nanocomposite derived a discharge capacity of *ca.* 130 mA h g⁻¹, approaching its theoretical value (133 mA h g⁻¹). At a high current rate (10 C), the nanocomposite also displayed an impressive long cycle life and remarkable capacity retention (90% after 1200 cycles) with a high Coulombic efficiency (>99%).

Results & discussion

The fabrication process and the detailed structure of our HN-LVP@C nanocomposite are schematically illustrated in Fig. 1a. The HN-LVP@C nanocomposite was synthesized *via* surfactant-assisted hydrothermal reaction with a carbothermal reduction technique. Polyethylene glycol (PEG), a non-ionic surfactant, was adopted as a surfactant in hydrothermal reaction,²⁵ and subsequently acted as both a reducing agent and a carbon source in the carbothermal reaction. The hydrothermal treatment generated a PEG-capped $\text{Li}_3\text{V}_2(\text{PO}_4)_3$ precursor, leaving some PEG content redundant due to its highly excessive amount in the start solution. Consequently, in the following carbothermal reaction, the $\text{Li}_3\text{V}_2(\text{PO}_4)_3$ precursor crystallized into a nanosphered “core” and the surface-adsorbed PEG carbonized into a carbon “shell”; meanwhile, the redundant PEG formed the surrounding 3D porous carbon matrix (the carbonization of chaotic PEG chains led to highly porous carbon networks) to produce the final HN-LVP@C nanocomposite. It is worth noting that our hybrid synthesis route has effectively combined the advantages of classical hydrothermal and

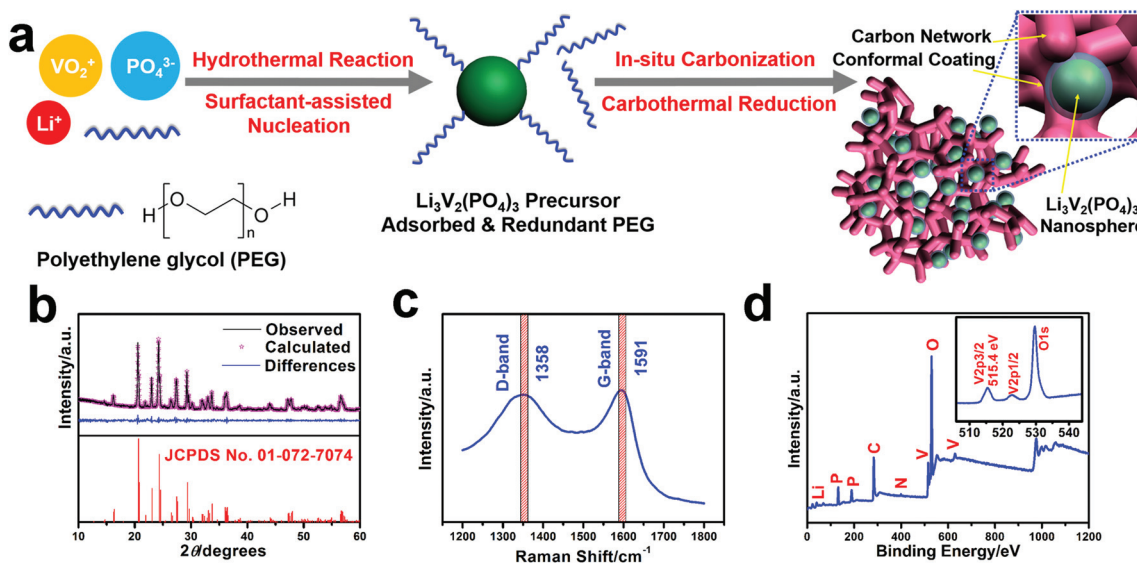


Fig. 1 (a) Schematic illustration of the formation of HN-LVP@C nanocomposite. (b) Rietveld refined XRD pattern, (c) Raman spectrum, and (d) survey XPS spectrum (inset: enlarged V 2p and O 1s regions) of the HN-LVP@C nanocomposite.

carbothermal reactions. In our case, the growth of $\text{Li}_3\text{V}_2(\text{PO}_4)_3$ crystal was significantly restricted by the carbon shell, resulting in nanosized spheres with high crystallinity, which would have been unattainable through either low-temperature hydrothermal approaches or ordinary solid-state reactions.

Fig. 1b shows the Rietveld refinement of the X-ray diffraction (XRD) data of the HN-LVP@C nanocomposite. As can be seen, all visible peaks in the spectrum can be readily assigned to the monoclinic $\text{Li}_3\text{V}_2(\text{PO}_4)_3$ (JCPDS card no. 01-072-7074, space group $P2_1/n(14)$), and the intense reflection peaks corroborate its high crystallinity. The calculated profile matches well with the observed one, with refined lattice parameters of $a = 8.648 \text{ \AA}$, $b = 8.634 \text{ \AA}$, $c = 12.096 \text{ \AA}$, and $\beta = 90.609^\circ$ (reliable factors $R_{\text{wp}} = 7.44\%$, and $S = 1.173$). The average crystallite size of $\text{Li}_3\text{V}_2(\text{PO}_4)_3$ was estimated to be $\sim 50 \text{ nm}$ by calculating the major diffraction peaks with Scherrer's formula. The existence of carbon content in the nanocomposite was verified by Raman measurements. As shown in Fig. 1c, the characteristic signatures at $\sim 1358 \text{ cm}^{-1}$ and $\sim 1591 \text{ cm}^{-1}$ are attributed to the D-band (disorder-induced phonon mode) and G-band (E_{2g} vibrations of graphite) of carbon, respectively.²⁶ In addition,

the peak intensity ratio of D and G bands ($I_{\text{D}}/I_{\text{G}}$) reflects the degree of crystallinity of various carbon materials. In our case, an $I_{\text{D}}/I_{\text{G}}$ value of ~ 1 demonstrates that the carbon content is fairly ordered, thereby implying good electron conductivity.²⁷ The combined XRD and Raman results suggest that the HN-LVP@C nanocomposite is composed of $\text{Li}_3\text{V}_2(\text{PO}_4)_3$ nanocrystals and well arranged carbon. Important information concerning the chemical composition and electronic structure as well as elemental valences was further extracted from X-ray photoelectron spectroscopy (XPS) as shown in Fig. 1d. The binding energy obtained in the XPS survey was corrected for specimen charging by referencing the C 1s line to 284.60 eV .²⁸ The V 2p core-level spectrum (see inset in Fig. 1d) confirms that the observed value of binding energies for V 2p_{3/2} and V 2p_{1/2} is consistent with the literature values for V^{3+} in bulk.²⁹ A rough atomic ratio of Li:V:P:O of about 3:2:3:12 was also obtained based on the quantification of the corresponding peaks, while the carbon content in the composite was determined to be $\sim 26 \text{ wt\%}$. A similar elemental composition was also obtained from inductively coupled plasma-optical emission spectrometry (ICP-OES) measurements.

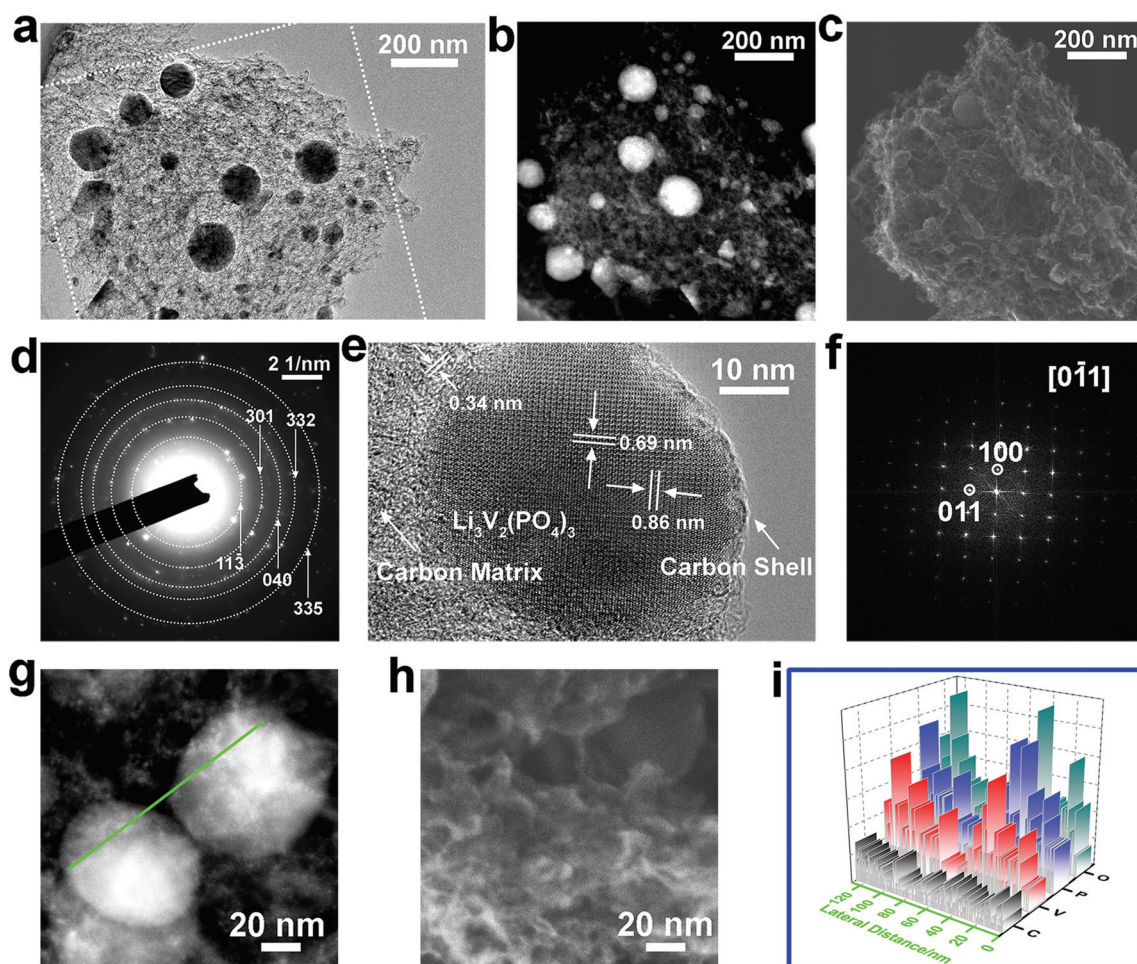


Fig. 2 (a) TEM micrograph, (b), (c), and (d) are the corresponding HAADF image, SEI image and SAED pattern, respectively. (b) and (c) are both acquired from the white-dashed square in (a). (e) High-resolution TEM image of a single nanosphere, and (f) the associated FFT pattern. (g) HAADF image from two adjacent nanospheres, (h) the corresponding SEI image, and (i) the cross-sectional EDS line profiles along the green line in (g).

The morphological and microstructural features of the HN-LVP@C nanocomposite were then characterized by transmission electron microscopy (TEM) and scanning electron microscopy (SEM). A bright-field TEM image, high-angle annular dark field (HAADF, Z-contrast image) image, and secondary electron image (SEI) at the STEM mode were sequentially captured from the same area as shown in Fig. 2a–c. It is evident from the images that the uniform nanospheres (30–100 nm) are evenly distributed inside a highly porous matrix (pore size: 3–20 nm). The selected area electron diffraction (SAED) pattern in Fig. 2d is well indexed to monoclinic $\text{Li}_3\text{V}_2(\text{PO}_4)_3$ (note: the multi-ring pattern was caused by the collective diffractions from many nanospheres, and the blurry intensity was brought by the diffused reflection from the carbon matrix). Upon examining a single nanosphere as presented in Fig. 2e, mutual-orthogonal 0.69/0.86 nm lattice fringes corresponding to the (011)/(100) planes (also see Fig. 2f – the associated fast Fourier transform (FFT) pattern) from the $\text{Li}_3\text{V}_2(\text{PO}_4)_3$ nanosphere can be indexed, as well as a partially ordered 0.34 nm lattice fringe (corresponding to the d -spacing of graphite (002) planes) from the surrounding carbon matrix. Notably, each $\text{Li}_3\text{V}_2(\text{PO}_4)_3$ nanosphere possesses its conformal carbon coating (*ca.* 1–2 nm in thickness) among repeated observations (also see Fig. S4†). Consequently, the energy dispersive X-ray spectrum (EDS) was utilized to check the elemental distribution in the composite. Results from quantitative EDS analysis (Fig. S5†) show identical chemical compositions to that of XPS results. The cross-sectional EDS line profiles (Fig. 2i) over two adjacent nanospheres (see green line in Fig. 2g, Fig. 2h from SEI with the same area shown in Fig. 2g) also proves that the nanospheres are embedded inside the highly porous matrix) suggest a synchronized fluctuation of vanadium, phosphorus, and oxygen contents with the carbon content almost unchanged. In brief, all TEM analyses confirmed a hierarchical composite structure composed of porous carbon networks with embedded $\text{Li}_3\text{V}_2(\text{PO}_4)_3/\text{C}$ core-shell nanospheres.

Combining the TEM results with the SEM micrographs as shown in Fig. 3a, it is clear that the HN-LVP@C nanocomposite appears to be sub-micrometer or micrometer in size and irregular shape. It can be also observed that most $\text{Li}_3\text{V}_2(\text{PO}_4)_3$ nanospheres are well embedded inside the carbon “foam” yet a few nanospheres are exposed and block some pores (denoted by red arrows in Fig. 3b). To further investigate the pore structure and the Brunauer–Emmett–Teller (BET) surface area of the HN-LVP@C nanocomposite, nitrogen isothermal adsorption–desorption measurement was performed. The results are presented in Fig. 3c, showing typical type-IV isotherm, a nanoporous characteristic, with a BET surface area of $69 \text{ m}^2 \text{ g}^{-1}$. The corresponding Barrett–Joyner–Halenda (BJH) pore-size distribution (Fig. 3c, inset) suggests the continuous existence of pores ranging from mesopores to macropores, with two peaks centered at 4 and 23 nm, which is in accordance with the TEM result. This innovative meso–macro porosity is expected to facilitate the penetration of electrolyte and to afford ample interfacial contact and therefore vigorously

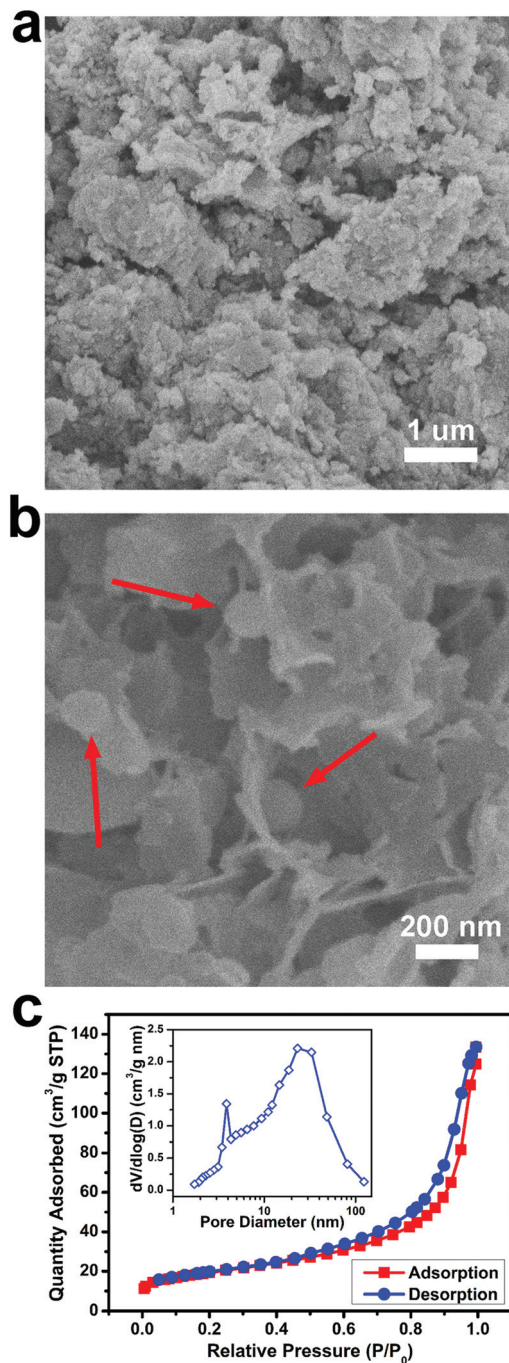


Fig. 3 Typical (a) low-magnification and (b) high-magnification SEM micrographs of the HN-LVP@C nanocomposite. (c) Nitrogen adsorption–desorption isotherms of the HN-LVP@C nanocomposite. Inset: the plot of pore-size distribution calculated by the BJH formula in the desorption branch isotherm.

promote the solid state diffusion kinetics of lithium intercalation.

The effect of the novel hierarchical carbon coating on the electrochemical performance of $\text{Li}_3\text{V}_2(\text{PO}_4)_3$ was thoroughly evaluated at room temperature with respect to Li^+ insertion/extraction using a coin-type half-cell, and the results are presented in Fig. 4. The electrochemical impedance spectroscopy

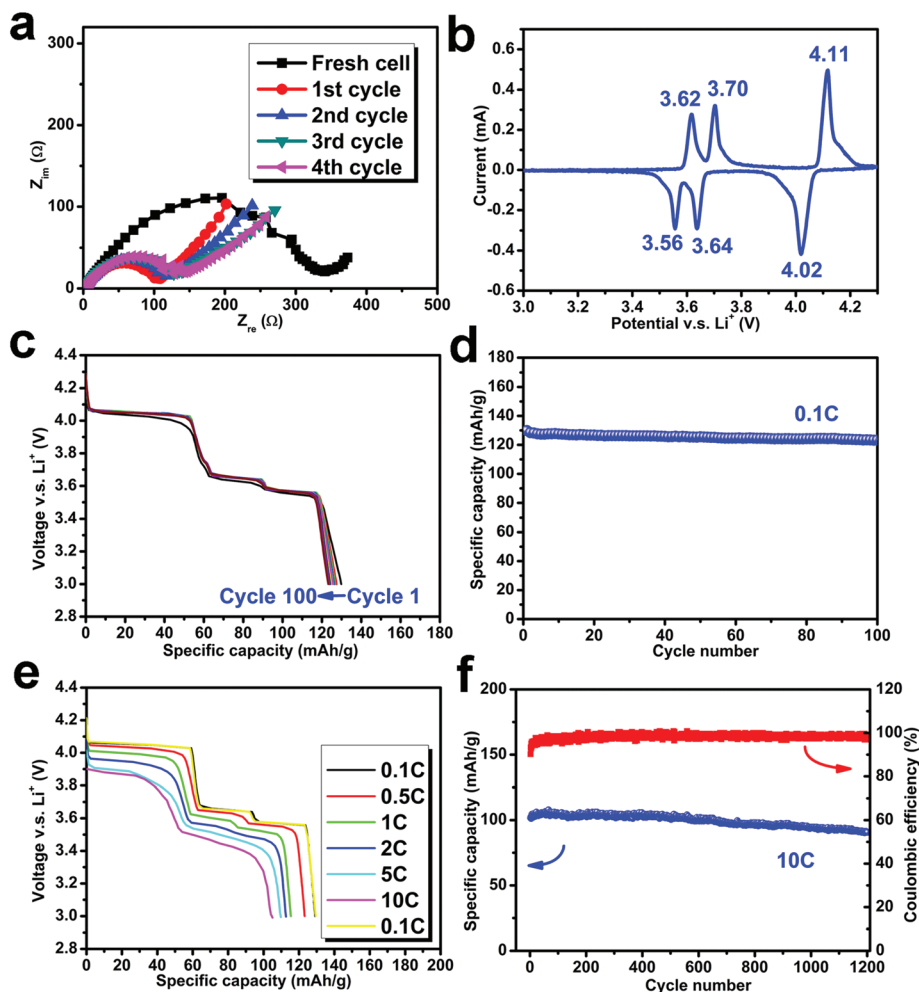


Fig. 4 Electrochemical performance of the HN-LVP@C nanocomposite tested between 3.0 and 4.3 V (versus Li/Li⁺) at room temperature. (a) EIS spectra in the frequency range between 0.1 Hz and 100 kHz with a vibration of 2 mV. (b) A typical CV profile at a scanning rate of 0.1 mV s⁻¹. (c) Discharge voltage profiles for cycles 1, 10, 20, 30, 40, 50, 60, 70, 80, 90, and 100 at 0.1 C. (d) Cycling performance at a rate of 0.1 C. (e) Rate capabilities with increasing rates from 0.1 C, 0.5 C, 1 C, 2 C, 5 C and 10 C at the first cycle, then back to 0.1 C. (f) Discharge capacity and Coulombic efficiency versus cycle number at a rate of 10 C.

(EIS) of the HN-LVP@C electrode was first performed on a freshly assembled cell and again after the 1st to 4th cycle to understand the electrolyte infiltration process during cell charge/discharge. As shown in the Nyquist plot in Fig. 4a, a decrease in the total resistance (*i.e.* resistance from the electrolyte, charge transfer and interfaces) was observed between the fresh cell and the subsequent curves, which could be ascribed to the increasing conductivity of the cathode after electrolyte infiltration. The diameters of the semicircles remain almost unchanged after the 1st cycle, implying the formation of a stable solid electrolyte interface caused by efficient electronic/ionic transport through the hierarchically porous electrodes upon cycling. Next, the cyclic voltammetry (CV) profile was recorded to gain deeper understanding on the charge/discharge process of the HN-LVP@C electrode between 3.0 and 4.3 V. As can be seen in Fig. 4b, three pairs of oxidation and reduction peaks could be clearly identified in the first cycle, which were consistent with previous reports.^{9,30} The first Li⁺

was extracted *via* two anodic peaks at 3.62 and 3.70 V, confirming the existence of an ordered Li_{2.5}V₂(PO₄)₃ intermediate phase and a Li₂V₂(PO₄)₃ phase. The second Li⁺ was then removed by one step at 4.11 V to form LiV₂(PO₄)₃. Three cathodic peaks located at 3.56, 3.64, and 4.02 V were observed as a result of the reinsertion of the two Li⁺ from the V⁴⁺/V³⁺ redox couple.

Subsequently, the representative discharge voltage profiles of the HN-LVP@C cathode at a current rate of 0.1 C (1 C = 133 mA g⁻¹) in the voltage window of 3.0–4.3 V were recorded and they are presented in Fig. 4c. Three clear plateaus at 4.04 V, 3.64 V, and 3.57 V were observed in each profile and the values are in good agreement with the CV test. The battery delivered an initial discharge capacity of *ca.* 130 mA h g⁻¹, approaching its theoretical value (133 mA h g⁻¹). The corresponding cycling performance at 0.1 C is shown in Fig. 4d and reveals an excellent cycling stability with a retention capacity of *ca.* 124 mA h g⁻¹ at the 100th cycle.

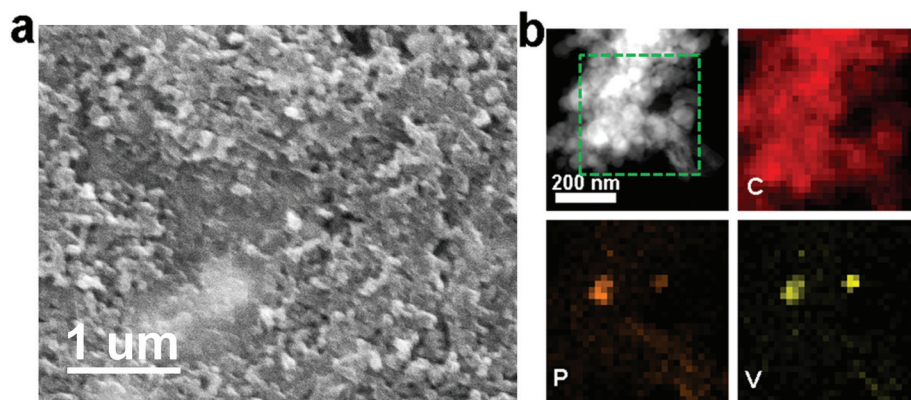


Fig. 5 (a) SEM image of the electrode after 1200 cycles, (b) HAADF image and the corresponding elemental mapping of the designated area (marked in a dashed square).

Today superior rate capability is highly desirable for cathode materials in high power LIB applications such as electric vehicles and hybrid electric vehicles. For this reason, the cycling responses of the nanocomposite cathode at high C rates were evaluated in our study. The results in Fig. 4e show that the HN-LVP@C cathode delivered a discharge capacity of 129.2 (0.1 C), 123.2 (0.5 C), 115.4 (1 C), 112.6 (2 C), 109.8 (5 C), 105.4 (10 C) gradually before returning to 129.4 mA h g⁻¹ (0.1 C), suggesting an excellent reversible rate performance. Surprisingly, our findings showed that the HN-LVP@C cathode possessed outstanding cycling stability at a high current rate with negligible capacity fading. After tolerating 1200 cycles at a rate of 10 C (Fig. 4f), the cathode retained a capacity retention of above 90%. It is worth noting that the Coulombic efficiency was constantly high (>99%) during the overall battery operation, indicating high reversibility at such a high current rate.

In comparison with other Li₃V₂(PO₄)₃ cathode materials with conductive coating reported in the literature (Table S1†), the quality of our HN-LVP@C nanocomposite is evidently superior, especially upon high-power usage. The exceptional performance can be contributed to the following structural factors. First, the high quality of crystallization, good dispersion and small sizes of the Li₃V₂(PO₄)₃ phase allow the full access of its maximum capacity. Second, the porous matrix of carbon functions as a three-dimensional buffer which accommodates the Li₃V₂(PO₄)₃ nanoparticles just like eggs packed in sponge packing foams. With such a buffering effect, the stress generated due to the volume change of Li₃V₂(PO₄)₃ caused by Li⁺ insertion/removal in the charging/discharging processes would become much localized and thus its ability to induce a phase change and/or decomposition of the nanoparticles would be significantly eliminated, resulting in high stability of the composite structures upon repeated charging/discharging. Third, the conductive and continuous carbon matrix and the surface carbon coating could enhance the efficient electrical connection between Li₃V₂(PO₄)₃ nanospheres. It is also important to note that the hierarchical carbon coating on the Li₃V₂(PO₄)₃ nanosphere also assists in forming a deformable and stable solid electrolyte interface, as shown in the SEM

image taken from the composite electrode after 1200 cycles (Fig. 5a), which is also favorable for good cycling stability. The TEM analysis (Fig. 5b) further suggests that not only the hierarchical carbon coating was well maintained, but the morphology and size of spherical Li₃V₂(PO₄)₃ nanoparticles were also greatly maintained after the deep cycling.

Conclusions

In summary, we demonstrated significantly enhanced electrochemical performance of Li₃V₂(PO₄)₃ *via* simultaneous size controlling and conductive coating in this work. The rational design and facile realization of a novel HN-LVP@C nanocomposite resulted in exceptional cycle stability and excellent high power capability, which can be directly ascribed to its unique microstructural merits. The remarkable performance derived from our simple and scalable synthesis suggests that this 4 V-class material could be one of the most promising candidates for future batteries.

Experimental section

Synthesis of the HN-LVP@C nanocomposite

A facile hydrothermal reaction followed by a solid-state carbothermal reduction synthesis was adopted in this work. Typically, V₂O₅ powders (4 mmol) and 40 ml H₂O were mixed under vigorous magnetic stirring at room temperature before 10 ml 30% H₂O₂ was slowly added to this mixture with continuous stirring for 30 min to form a transparent burgundy solution. After that, CH₃COOLi·2H₂O (12 mmol), NH₄H₂PO₄·2H₂O (12 mmol) and polyethylene glycol (PEG-600, 3 ml) were sequentially added to the solution, forming a light-yellow solution. The resulting solution was adjusted to a volume of 80 ml H₂O before it was transferred to a 100 ml autoclave. The autoclave was sealed and kept at 200 °C for 4 days before cooling down to room temperature naturally. The resulting brown gel-like residue was dried in an electronic oven at 100 °C overnight

and grounded thoroughly before it was delivered to the heating process. To form the HN-LVP@C nanocomposite, the precursor was first heated (heating rate $5\text{ }^{\circ}\text{C min}^{-1}$) in a tube furnace at $450\text{ }^{\circ}\text{C}$ for 2 h, followed by milling and then heated at $850\text{ }^{\circ}\text{C}$ for 12 h (Fig. S6†). The whole process was protected by a constant argon flow. After cooling ($10\text{ }^{\circ}\text{C min}^{-1}$) to room temperature, the products were obtained by collecting the as-heated powder (see Fig. S7†).

Structural characterizations

Simultaneous thermogravimetric analysis & differential scanning calorimetry (TG–DSC) analysis were performed on a NETZSCH STA 449 C Jupiter® system under flowing argon. Powder XRD measurement was taken using a Rigaku SmartLab Intelligent X-ray diffraction system with filtered Cu K_{α} radiation ($\lambda = 1.5406\text{ \AA}$, operating at 45 kV and 200 mA). Rietveld refinement of the XRD profile was calculated by an integrated X-ray Powder Diffraction Software Package (PDXL Ver. 1.8.1.0, Rigaku). Raman measurement was taken using a Horiba Jobin Yvon LabRAM HR System with a laser wavelength of 488 nm. XPS measurement was made on an ESCALab 250 (Thermo-VG Scientific) X-ray photoelectron spectrometer with an Al K_{α} excitation source. ICP-OES was conducted on a PerkinElmer Optima 7300 DV Spectrometer. TEM images and EDS were recorded through a JEM 2100F (field emission) scanning transmission electron microscope equipped with an Oxford INCA x-sight EDS Si(Li) detector at an acceleration voltage of 200 kV. SEM observations were made on a JEOL 6335F system (operating at 5–10 kV). The nitrogen adsorption and desorption isotherms at 77.3 K were obtained with a Micromeritics TriStar II 3020 M Physisorption system.

Electrochemical measurements

Electrochemical performance measurements were taken using 2016 coin-type half-cells assembled in a glove box filled with protective argon gas (M. Braun Inert Gas Systems Co. Ltd, Germany). The cathodes of the test cells were made from the active material, conductive Super P, and a poly(vinyl difluoride) binder in a weight ratio of 80 : 10 : 10. The cathode slurry was prepared by thoroughly mixing a *N*-methyl-2-pyrrolidone solution with the active material, Super P, and a poly(vinyl difluoride) binder. Consequently, the resulting slurry was deposited on aluminum foil (20 μm) and pressed before the entire assembly was dried in a vacuum oven at $120\text{ }^{\circ}\text{C}$ overnight. The average loading of the electrode is around $3.8\text{--}5.1\text{ mg cm}^{-2}$. A pure lithium foil was used as the anode, and a polypropylene separator (Celgard 2400) was used to separate the cathode and the anode. A 1 M LiPF_6 solution in ethylene carbonate and diethyl carbonate mixed at a weight ratio of 1 : 1 was adopted as the electrolyte in the test cells. The EIS and CV performances were tested using a Potentiostat/Galvanostat (EG&G Princeton Applied Research 273A). The discharge and charge measurements were made on a Land battery test system (Wuhan L and Electronic Co., China) in a voltage window of 3.0–4.3 V at room temperature at different rates. The charge and discharge tests were carried out under same currents.

Acknowledgements

This work was supported by the Hong Kong Polytechnic University (A-PK29, A-PL53 and 1-ZVAW).

Notes and references

- 1 B. Scrosati, *Nature*, 1995, **373**, 557–558.
- 2 A. S. Aricò, P. Bruce, B. Scrosati, J.-M. Tarascon and W. van Schalkwijk, *Nat. Mater.*, 2005, **4**, 366–377.
- 3 B. Dunn, H. Kamath and J.-M. Tarascon, *Science*, 2011, **334**, 928–935.
- 4 M. S. Whittingham, *Chem. Rev.*, 2004, **104**, 4271–4302.
- 5 L. Fei, W. Lu, L. Sun, J. Wang, J. Wei, H. L. W. Chan and Y. Wang, *RSC Adv.*, 2013, **3**, 1297.
- 6 J. Kim, J. K. Yoo, Y. S. Jung and K. Kang, *Adv. Energy Mater.*, 2013, **3**, 1004–1007.
- 7 H. Huang, S. C. Yin, T. Kerr, N. Taylor and L. F. Nazar, *Adv. Mater.*, 2002, **14**, 1525–1528.
- 8 M. M. Ren, Z. Zhou, X. P. Gao, W. X. Peng and J. P. Wei, *J. Phys. Chem. C*, 2008, **112**, 5689–5693.
- 9 H. Liu, P. Gao, J. Fang and G. Yang, *Chem. Commun.*, 2011, **47**, 9110–9112.
- 10 C. Liu, F. Li, L.-P. Ma and H. M. Cheng, *Adv. Mater.*, 2010, **22**, E28–E62.
- 11 H.-K. Song, K. T. Lee, M. G. Kim, L. F. Nazar and J. Cho, *Adv. Funct. Mater.*, 2010, **20**, 3818–3834.
- 12 C. Sun, S. Rajasekhara, Y. Dong and J. B. Goodenough, *ACS Appl. Mater. Interfaces*, 2011, **3**, 3772–3776.
- 13 Y. Wang, P. He and H. Zhou, *Energy Environ. Sci.*, 2011, **4**, 805–817.
- 14 N. Ravet, Y. Chouinard, J. F. Magnan, S. Besner, M. Gauthier and M. Armand, *J. Power Sources*, 2001, **97–98**, 503–507.
- 15 Z. Chen, Y. Qin, K. Amine and Y.-K. Sun, *J. Mater. Chem.*, 2010, **20**, 7606–7612.
- 16 H. Liu, G. Yang, X. Zhang, P. Gao, L. Wang, J. Fang, J. Pinto and X. Jiang, *J. Mater. Chem.*, 2012, **22**, 11039–11047.
- 17 B. Liu, P. Soares, C. Checkles, Y. Zhao and G. Yu, *Nano Lett.*, 2013, **13**, 3414–3419.
- 18 H. Wu, G. Yu, L. Pan, N. Liu, M. T. McDowell, Z. Bao and Y. Cui, *Nat. Commun.*, 2013, **4**, 1943.
- 19 Q. Chen, T. Zhang, X. Qiao, D. Li and J. Yang, *J. Power Sources*, 2013, **234**, 197–200.
- 20 W. Duan, Z. Hu, K. Zhang, F. Cheng, Z. Tao and J. Chen, *Nanoscale*, 2013, **5**, 6485–6490.
- 21 L. Mai, S. Li, Y. Dong, Y. Zhao, Y. Luo and H. Xu, *Nanoscale*, 2013, **5**, 4864–4869.
- 22 L. L. Zhang, G. Liang, G. Peng, F. Zou, Y. H. Huang, M. C. Croft and A. Ignatov, *J. Phys. Chem. C*, 2012, **116**, 12401–12408.
- 23 C. Wang, H. Liu and W. Yang, *J. Mater. Chem.*, 2012, **22**, 5281–5285.
- 24 A. Pan, J. Liu, J. G. Zhang, W. Xu, G. Cao, Z. Nie, B. W. Arey and S. Liang, *Electrochem. Commun.*, 2010, **12**, 1674–1677.

- 25 L. Fei, J. Yuan, Y. Hu, C. Wu, J. Wang and Y. Wang, *Cryst. Growth Des.*, 2011, **11**, 1049–1053.
- 26 A. Ferrari and J. Robertson, *Phys. Rev. B: Condens. Matter*, 2000, **61**, 14095–14107.
- 27 T. Muraliganth, A. Vadivel Murugan and A. Manthiram, *Chem. Commun.*, 2009, 7360–7362.
- 28 C. Z. Wu, Y. Xie, L. Y. Lei, S. Q. Hu and C. Z. OuYang, *Adv. Mater.*, 2006, **18**, 1727–1732.
- 29 G. Sawatzky and D. Post, *Phys. Rev. B: Condens. Matter*, 1979, **20**, 1546–1555.
- 30 S. C. Yin, H. Grondey, P. Strobel, M. Anne and L. F. Nazar, *J. Am. Chem. Soc.*, 2003, **125**, 10402–10411.